ACS APPLIED MATERIALS & INTERFACES

Research Article

www.acsami.org

Fabrication of $CuInS_2$-Sensitized Solar Cells via an Improved SILAR Process and Its Interface Electron Recombination

Xueqing Xu,*[,†,‡] Qingcui Wan,[†,‡] Chunyan Luan,[§] Fengjiao Mei,[†] Qian Zhao,[†,‡] Ping An,[†,‡] Zhurong Liang,[†,‡] Gang Xu,[†,‡] and Juan Antonio Zapien*[,§]

[†]CAS Key Laboratory of Renewable Energy, Guangzhou Institute of Energy Conversion, Chinese Academy of Sciences, Guangzhou 510640, People's Republic of China

[‡]University of Chinese Academy of Sciences, Beijing 100049, People's Republic of China

[§]Department of Physics and Materials Science and Centre for Functional Photonics, City University of Hong Kong, New Kowloon, Hong Kong SAR

Supporting Information

ABSTRACT: Tetragonal $CuInS_2$ (CIS) has been successfully deposited onto mesoporous TiO_2 films by in-sequence growth of In_xS and Cu_yS via a successive ionic layer absorption and reaction (SILAR) process and postdeposition annealing in sulfur ambiance. X-ray diffraction and Raman measurements showed that the obtained tetragonal CIS consisted of a chalcopyrite phase and Cu−Au ordering, which related with the antisite defect states. For a fixed Cu−S deposition cycle, an interface layer of β-In_2S_3 formed at the TiO_2/CIS interface with suitable excess deposition of In−S. In the meantime, the content of the Cu−Au ordering phase decreased to a reasonable level. These facts resulted in the retardance of electron recombination in the cells, which is proposed to be dominated by electron transfer from the conduction band of TiO_2 to the unoccupied defect states in CIS via exponentially distributed surface states. As a result, a relatively high efficiency of ~0.92% (V_{oc} = 0.35 V, J_{sc} = 8.49 mA cm^{-2}, and FF = 0.31) has been obtained. Last, but not least, with an overloading of the sensitizers, a decrease in the interface area between the sensitized TiO_2 and electrolytes resulted in deceleration of hole extraction from CIS to the electrolytes, leading to a decrease in the fill factor of the solar cells. It is indicated that the unoccupied states in CIS with energy levels below E_{F0} of the TiO_2 films play an important role in the interface electron recombination at low potentials and has a great influence on the fill factor of the solar cells.

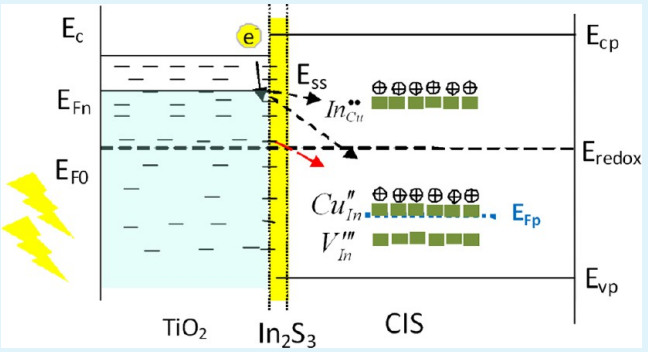

KEYWORDS: *$CuInS_2$, sensitized solar cells, fabrication, successive ionic layer absorption and reaction (SILAR), electron recombination*

1. INTRODUCTION

Extremely thin absorber solar cells based on mesoporous wide-band-gap semiconductor (WBSC) films sensitized with organic and inorganic absorbers have attracted great attention because of their effective charge separation at the WBSC/absorber interface,[1] which allows the use of low-cost materials with more defects than the thin-film solar cells. Accordingly, nanocrystalline inorganic semiconductor absorbers (QDs or ultrathin films) can be prepared in a relatively simple way and present many other attractive advantages, such as tunable band gaps, high extinction coefficients, large intrinsic dipole moments, etc.[2,3] The most commonly used inorganic absorbers are II−VI, III−V, and ternary I−III−IV semiconductors, such as CdSe, CdS, PbSe, PbS, InAs, Bi_2S_3, and $CuInS_2$ (copper indium sulfide, CIS). In particular, $CuInS_2$ is of great interest because of many attractive features including (i) nontoxicity and abundance on Earth, (ii) a high absorption coefficient (6×10^5 cm^{-1}) and a direct band gap of 1.5 eV well matched to the solar spectrum,[4] and (iii) appreciable photoelectrochemical stability in polysulfide electrolytes, which are widely used as hole-transport materials.

Several approaches have been employed to deposit inorganic photosensitizers on TiO_2 films, including presynthesized colloidal QDs (CQDs), chemical bath deposition,[5] successive ionic layer absorption and reaction (SILAR),[6] electrophoresis deposition,[7] and thermal decomposition[8] among others. A power conversion efficiency (PCE) of ~4.2% has been reported for CQD CIS-sensitized solar cells,[9] and recently a higher PCE of ~5.3% has been achieved when CQD CIS was coated with Mn-doped CdS.[10] Feng et al. attempted to deposit CIS nanoparticles onto the mesoporous TiO_2 films by the solvothermal method;[11] however, the CIS nanoparticles were

Received: June 27, 2013
Accepted: October 17, 2013
Published: October 17, 2013

found to precipitate or simply deposit onto the surface of the TiO_2 films. Atomic layer chemical vapor deposition (ALCVD) has been used to obtain In_2S_3/CIS-coated TiO_2 films with a relatively high PCE of ~4% for all-solid-state solar cells.[12] However, ALCVD is a relatively expensive technique that results in small deposition rates. Spray pyrolysis has also been used to grow p-type CIS on TiO_2 films at 370 °C in an ambient atmosphere, resulting in a PCE of ~5%;[12] in this case, however, KCN etching was needed to remove excess copper sulfide phase followed by a postdeposition annealing at 525 °C in a H_2S atmosphere.

The SILAR process presents many advantages such as high surface coverage, controllable thickness of the nanoparticle layers, and simple equipment requirements. However, the PCE of the CIS-sensitized solar cells based on the SILAR process is still very low. Wu et al. employed the SILAR process to deposit a CIS nanotube array on indium−tin oxide films using ZnO nanowires as templates followed by annealing in sulfur ambient at 500 °C. This resulted in Cu-rich p-type CIS-based solar cells with PCE ~ 0.47% [V_{oc} = 0.33 V, J_{sc} = 5.52 mA cm^{-2}, and fill factor (FF) = 0.26].[13] In a different report, Chang et al. adopted a modified SILAR method (so-called ionic compound lamination reaction) to prepare CIS on titania nanotube arrays and obtained an extremely lower current density of ca. 300 mA cm^{-2}[14] (and the PCE has not been reported). Very recently, Wu and Zhou et al. has fabricated CIS-sensitized TiO_2 nanorod films via a conventional SILAR process. With optimization of CIS SILAR cycles and the introduction of a In_2S_3 buffer layer, QD-sensitized solar cells assembled with a 3-μm-thick TiO_2 nanorod film exhibited a PCE of ~1.06%.[15] Clearly, much effort is still needed to achieve the expected PCE performance that can be expected from CIS-based solar cells. In this paper, CIS has been deposited onto mesoporous TiO_2 by an improved SILAR process, i.e., in situ growth of In_xS and Cu_yS via the SILAR process followed by postdeposition annealing at 550 °C and low pressure under a sulfur environment. Compared with a conventional SILAR process, this improved SILAR process is more facile, and it is easier to control the chemical composition and the grain size of the CIS and also the thickness of the In_2S_3 buffer layer by adjusting the number of the In−S and Cu−S deposition cycles, as we described in the following text. It was found that a suitable excess of In−S deposition cycles resulted in the formation of In_2S_3 at the TiO_2/CIS interface and a decrease in the defect states in CIS, which resulted in retardance of the interface electron recombination and great improvement of the photovoltaic performance of the solar cell. As a consequence, a PCE of ~0.92% (V_{oc} = 0.35 V, J_{sc} = 8.49 mA cm^{-2}, and FF = 0.31) has been obtained. This is a relatively high PCE value for CIS-sensitized solar cells based on the SILAR process. On the other hand, with an overexcess of In−S deposition cycles, FF and J_{sc} of the solar cells decreased. In order to obtain a deep understanding of the photovoltaic performance of the solar cells, the interface electron recombination mechanism of the solar cells has been investigated.

2. EXPERIMENT

2.1. Preparation of $CuInS_2$-Sensitized TiO_2 Electrodes. Cleaned FTO/glass substrates were used; first, a compact layer of TiO_2 films (~100 nm thick) was deposited by spray pyrolysis of titanium(IV) bis(acetoacetonato)diisopropanoxylate to retard the electron recombination at the FTO glass/electrolytes interface.[16] On the top of this compact layer, a transparent mesoporous TiO_2 film composed of 20 nm TiO_2 particles was prepared using the doctor blade method; the TiO_2 paste was purchased from Hepta Chroma in China. The films were then sintered at 450 °C for 30 min followed by treatment in an aqueous $TiCl_4$ solution (30 mM) at 75 °C. The thickness of the transparent mesoporous TiO_2 film is about 5 μm. The electrodes were sensitized with CIS via in situ deposition of In_xS followed by Cu_yS via the SILAR process. The precursor solutions for In, Cu, and S were 0.01 M CuCl, 0.075 M $Na_2S{\cdot}9H_2O$/buffer, and 0.1 M $InCl_3$ aqueous solutions, respectively. A buffer composed of 0.1 M $KH_2(PO_4)$ and 0.1 M NaOH was prepared for a Na_2S solution according to the literature.[13] For In_xS growth, the TiO_2 electrodes were successively immersed in the following solutions for different times: $InCl_3$ aqueous (60 s), ultrapure water (R = 18.2 MΩ·cm) (30 s), $Na_2S{\cdot}9H_2O$/buffer (240 s), and ultrapure water (30 s). This process was repeated for several cycles to form In_xS. Then Cu_yS was deposited as follows: immersing the sample into aqueous CuCl (30 s), ultrapure water (30 s), $Na_2S{\cdot}9H_2O$/buffer (240 s), and ultrapure water (30 s) in sequence. This process was repeated for several cycles to form Cu_yS. After the SILAR process, the sensitized TiO_2 electrodes were annealed at low pressure and 550 °C in sulfur ambient. After sensitization, the samples were further coated with ZnS by twice dipping them alternately into 0.1 M Zn $(CH_3COO)_2$ and 0.1 M Na_2S solutions for 1 min dip^{-1}.

2.2. Solar Cell Configuration. The cells were prepared by assembling the counter electrode and a QD-sensitized electrode using a scotch spacer and a polysulfide electrolyte. The polysulfide electrolyte was prepared with a 1 M Na_2S, 1 M S, and 0.1 M NaOH solution in 10 mL of Milli-Q ultrapure water. The Cu_2S counter electrodes were prepared by immersing brass in a HCl solution at 70 °C for 45 min and subsequently dropping a polysulfide electrolyte onto them for 10 min, resulting in porous Cu_2S electrodes. The area of the cells was 0.24 cm^2.

2.3. Characterization. X-ray diffraction (XRD) patterns were obtained on an X'pert pro MPD X-ray diffractometer using Cu Kα irradiation at a scan rate (2θ) of 0.00167° s^{-1}. The accelerating voltage and applied current were 40 kV and 80 mA, respectively. Energy-dispersive X-ray (EDX) spectra were performed on a Hitachi S-4800 field emission scanning electron microscope with an Oxford instruments Inca EDX system operated at 20 kV. High-resolution transmission electron microscopy (HRTEM) images were obtained with a Philips CM200 FEG TEM operated at 200 kV. Raman spectra of the CIS-coated TiO_2 films were detected on a LabRAM HR800 with an excitation wavelength of 532 nm. Scanning electron microscopy (SEM) images were obtained on a Hitachi S-4800 field emission scanning electron microscope. The diffuse reflection and transmission spectra of the CIS-sensitized TiO_2 electrodes have been measured on a Shimadzu UV-2401 UV−vis spectrophotometer with an integrating sphere. The spectra were measured with the FTO glass sides facing the light and with the TiO_2 electrodes before being sensitized as blanks. The absorption spectra of the samples were obtained according to absorption (%) = 100% − transmittance (T) − reflectance (R). Photocurrent−potential (J−V) and open-circuit voltage decay measurements were obtained with a FRA-equipped type III electrochemical workstation from Autolab. The cells were illuminated using the ABET Sun 3000 solar simulator at AM1.5G, where the light intensity was adjusted with an NREL-calibrated Si solar cell to one sun light intensity (100 mW cm^{-2}).

3. THEORETICAL BASIS ON THE J−V EQUATION AND INTERFACE ELECTRON RECOMBINATION

Figure 1a presents the equivalent circuit of the solar cells. From Figure1a, it can be seen that

$$J = J_{sc} - J_{re} \quad (1)$$

That is to say, the current density of the solar cells depends on the short-circuit current density, J_{sc}, and the recombination current density, J_{re}. J_{sc} is the maximum of the photogenerated carrier per unit that is extracted from the solar cells, which is

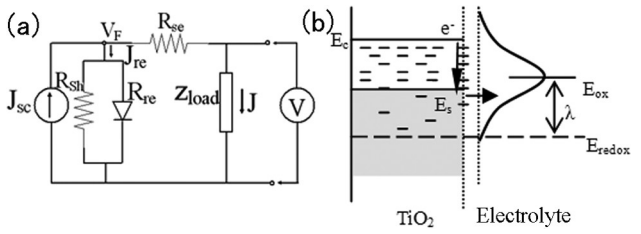

Figure 1. (a) Standard equivalent circuit for the solar cells. (b) Schematic maps of the recombination between the electrons in TiO_2 nanoparticles captured by the surface states and the holes in the electrolytes.

determined by the light-harvesting efficiency, η_{LH}, photoelectron injection efficiency, η_{inj}, and photoelectron collection efficiency, η_{col},

According to the interfacial electron recombination mechanism (as shown in Figure 1b) of differential scanning calorimetry (DSC) suggested by Bisquert et al.,[9] i.e., electron transfer from an exponentially distributed surface state of WBSC toward an acceptor in the electrolyte with a reorganization energy of λ, the recombination current density, J_{re}, can be expressed as follows:

$$J_{re} = J_0 \int_0^{V_F} \exp\left[-\frac{(qV_F - E_\mu)^2}{4\lambda kT}\right] dV \quad (2)$$

where V_F is the voltage drop in the sensitized TiO_2 films, k is the Boltzmann constant, and T is the absolute temperature. The electron recombination at the WBSC/absorber/electrolyte interfaces could also be quantitatively described by the electron recombination resistance, R_{re}. It has the following relationship with J_{re}:[17]

$$R_{re}^{-1} = \frac{dJ_{re}}{dV} \quad (3)$$

So

$$R_{re} = R_{remin} \exp\left[\frac{(qV_F - E_\mu)^2}{4\lambda kT}\right] \quad (4)$$

Equation 4 shows that the R_{re} dependence on the voltage consists of a Gaussian function centered at the energy of E_μ, and a minimum of the recombination resistance, R_{remin}, appeared at $qV_F = E_\mu$.

If $qV_F \ll E_\mu$, eqs 2 and 4 could be further approximated as an exponential dependence as follows:

$$J_{re} = J_{re0}\left[\exp\left(\frac{\beta qV_F}{kT}\right) - 1\right] \quad (5)$$

$$R_{re} = R_{re(V_F=0)} \exp\left(\frac{-\beta q}{kT}V_F\right) \quad (6)$$

where J_{re0} is the reverse saturation current density, $R_{re(V_F=0)}$ is the recombination resistance at V_F = 0 V, and β can be expressed as follows:

$$\beta = \frac{E_\mu}{2\lambda} \quad (7)$$

From eq 5, eq 1 could be expressed as follows:

$$J = J_{sc} - J_{re0}\left[\exp\left(\frac{\beta qV_F}{kT}\right) - 1\right] = J_{sc} - J_{re0}\left[\exp\left(\frac{q(V + JR_{se})}{mkT}\right) - 1\right] \quad (8)$$

Equation 8 is the typical $J-V$ equation for the solar cells, where $m = 1/\beta$, $V_F = V + JR_{se}$, m is the ideality factor of the solar cells, R_{se} is the series resistance, and both of them have an inverse relationship with FF of the solar cells. It can be seen that FF would decrease when β decreases. In another words, β is an important parameter that reflects FF of the solar cells.

4. RESULTS AND DISCUSSION

4.1. Phase Composition Analysis. In order to obtain CIS-sensitized TiO_2 electrodes, In_xS and Cu_yS were successively deposited onto the mesoporous TiO_2 films via the SILAR process with postdeposition annealing. We have tried to treat the CIS films at different temperatures. It was found that the CIS films treated at 550 °C had the best crystallinity and owned the best photovoltaic performance. The obtained samples were named as In*a*Cu*b*, where *a* and *b* represent the number of deposition cycles of In−S and Cu−S. The phase composition of the CIS films was heavily influenced by the deposition sequence and the deposition cycle of In−S and Cu−S. It was found that when Cu_yS was deposited prior to In_xS, the XRD peak of CIS was very weak because of sublimation of In_xS during annealing under low pressure. In this work, to prevent sublimation of In_xS, In_xS was deposited prior to Cu_yS. In addition, In_xS can prevent contamination of TiO_2 by copper ions. Figure 2a presents the XRD patterns of the sensitized TiO_2 electrodes annealed in sulfur ambient at 550 °C. The spectra consist of diffraction peaks corresponding to the FTO substrate (circles) and anatase TiO_2 (squares) and diffraction peaks at 27.87°, 32.38°, 46.44°, and 55.08° associated with the (112), (200)/(004), (204), and (312) crystal planes of tetragonal CIS (PDF 27-0159), in agreement with the results from Goossens et al.[12] In addition, the two weak peaks at 27.4° and 33.5° shown in the inset pattern for sample In11Cu5 could be attributed to the (109) and (0012) crystal planes of β-In_2S_3 (PDF 25-0390),[18] as observed in the pattern of sample In12Cu0.

Before annealing, only one peak at 27.4° associated with β-In_2S_3 can be observed (as shown in the Supporting Information Figure S1), which indicated that CIS has not been formed in the as-deposited films. With annealing at 550 °C in the sulfur ambient, In_2S_3 reacted with Cu_2S, resulting in the formation of CIS films,[19] which might be expressed as follows:

$$In_2S_3 + Cu_2S = 2CuInS_2 \quad (9)$$

In fact, the formation and growth mechanism of CIS is complex and needs to be further investigated. As shown in Figure 2a, for the In5Cu5 samples, the diffraction peaks of CIS were very weak. When the deposition cycles of In−S reached 8, the (112) and (204) peaks at 27.87° and 46.44°, respectively, became stronger and sharper, and the diffraction peak of the β-In_2S_3 phase appeared, which suggested that an interface layer of In_2S_3 formed between TiO_2 and CIS. According to the Scherrer equation, the grain size perpendicular to the (112) and (204) crystal planes has been calculated, and the results are listed in Table 1. It can be seen that the grain size of CIS increased with the In−S deposition cycle at first and reached an optimum value between 8 and 10 cycles. However, the values of the grain

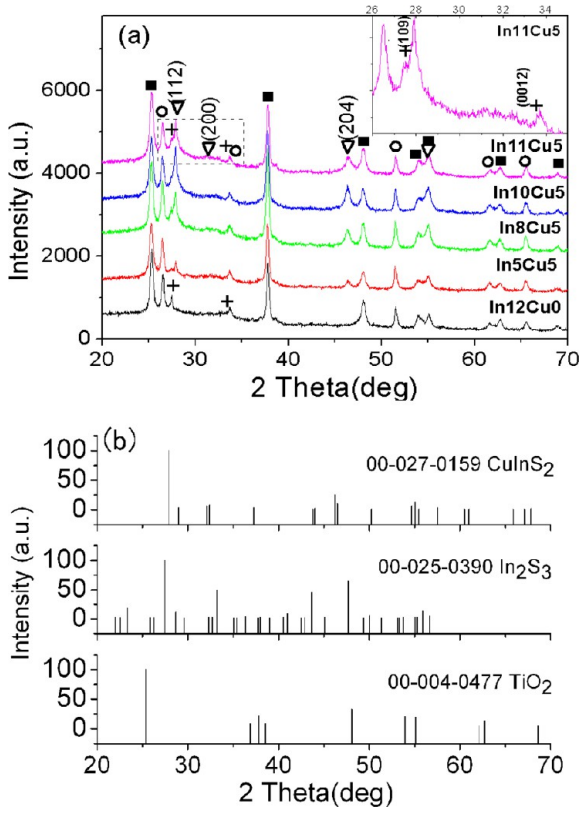

Figure 2. (a) XRD patterns of the sensitized TiO_2 electrodes with postdeposition annealing in sulfur ambiance: (■) TiO_2; (○) SnO_2; (▽) CIS; (+) In_2S_3. (b) Standard patterns of CIS, In_2S_3, and TiO_2.

size calculated from XRD measurements were much larger than those from the HRTEM measurements.

In addition, the element compositions of the CIS-sensitized TiO_2 films have been detected by using EDX spectral measurements, and the molar ratio of $TiO_2/In_2S_3/CuInS_2$ has been estimated. As shown in Table 1, for the In5Cu5 samples, Cu-rich CIS has been formed, which indicated that a portion of In has been sublimated under low pressure. It can be imagined that there were lots of In vacancies in the In5Cu5 samples. With an increase in the In−S deposition cycles, the content of the In and S elements increased, leading to an increase in the molar ratio of In_2S_3 to TiO_2, which implied that the thickness of the In_2S_3 buffer layer increased. It also can be seen that the content of the Cu element remained nearly constant until the In−S deposition cycles achieved 10 and then decreased, which should result from a decrease in the diffusion rate of the Cu^+ ions with a decrease in the diffusion path in the TiO_2 films. That is why the grain size of CIS decreased after the In−S deposition cycles were above 10.

Further, the detailed morphology and crystalline structure of the CIS-sensitized TiO_2 films have been observed by using HRTEM measurements. Figure 3 presents the typical HRTEM images for the In5Cu5 and In11Cu5 samples. As shown in Figure 3a, the TiO_2 films were covered with CIS nanoparticles with sizes of 3−5 nm. The observed lattice spacing distance of 0.355 nm belongs to the TiO_2 matrix. The observed lattice spacing distances of about 0.320 and 0.280 nm correspond to the (112) and (200) planes of the tetragonal CIS. These results were well matched with the XRD patterns, although the diffraction peak of the (200) plane was very weak. In comparison with the In5Cu5 samples, as shown in Figure3c, there appeared an interface layer of thickness of about 1 nm between TiO_2 and CIS for the In11Cu5 samples. The lattice fringe with a distance of 0.270 nm could be attributed to the (0012) plane of β-In_2S_3. The grain size of CIS perpendicular to the (112) planes for the In5Cu5 and In11Cu5 samples is listed in Table 1. The values were much smaller than those derived from XRD analysis. Furthermore, there existed some particles with lattice fringes not continuous, which suggested that the particles consisted of polycrystalline CIS, the crystal quality was not perfect, and there existed some grain boundaries.

In CIS materials, one may expect the coexistence of two phases: one is chalcopyrite-ordered and the other one is Cu−Au-ordered. The latter one is derived from the chalcopyrite-ordered phase and related with the antisite defect states, Cu_{In}'' and In_{Cu}'', which can cause electron recombination and limit the performance of the solar cells. In order to get more information on the phase composition of the prepared samples, Raman spectra of the sensitized TiO_2 electrodes have been detected, as shown in Figure 4a. Apart from the Raman peaks attributed to the anatase TiO_2, the peaks between 290 and 310 cm^{-1} related to CIS have been fitted with Lorentzian peaks for samples In8Cu5 and In10Cu5, as presented in Figure 4b,c. The results show that the most intense Raman band consists of two bands: the A_1 band of the chalcopyrite-ordered compound at 290 cm^{-1} and the A_1* band of Cu−Au ordering at 300 cm^{-1}.[20] When In10Cu5 is compared with In8Cu5, the intensity of the A_1 mode of the chalcopyrite ordering became stronger than that of the A_1* mode of the Cu−Au-ordered phase, which indicated that there existed a higher content of the Cu−Au-ordered phase and antisite defect states in In8Cu5 than in In10Cu5. On the other hand, it can be seen that the In11Cu5 and In12Cu5 samples have content similar to that of the Cu−Au-ordered phase as In10Cu5 samples. In addition, the intensive Raman bands at 330 and 324 cm^{-1} could belong to the E_{LO}^1 and B_2^1 modes of the chalcopyrite structure, respectively. The shoulder peaks around 308 and 314 cm^{-1} for In8Cu5 and In10Cu5, respectively, could be assigned to the A_{1g} mode of β-In_2S_3[21] as the peak at around 310 cm^{-1} observed in In12Cu0.

Table 1. Composition, Grain Size, and Optical Band Gap of the CIS Obtained with Different In−S Deposition Cycles

	XRD		TEM	EDX					EDX	UV−vis	
	(112) (nm)	(204) (nm)	size (nm)	Cu (atom %)	In (atom %)	S (atom %)	Ti (atom %)	O (atom %)	$TiO_2/In_2S_3/CuInS_2$ (molar ratio)	E_g (eV)	size (nm)
In5Cu5	10.8	8.7	3-5	3.38	3.27	7.48	24.79	60.44	100/-/13.63	1.74	5−6
In8Cu5	12.1	14.4		2.83	5.29	9.28	21.57	61.24	100/6.08/12.90	1.77	
In10Cu5	15.6	14.3		3.00	6.73	12.80	21.36	60.57	100/8.73/14.04	1.85	
In11Cu5	14.1	11.2	3-6	3.20	8.22	13.43	26.58	59.48	100/9.44/12.04	1.98	

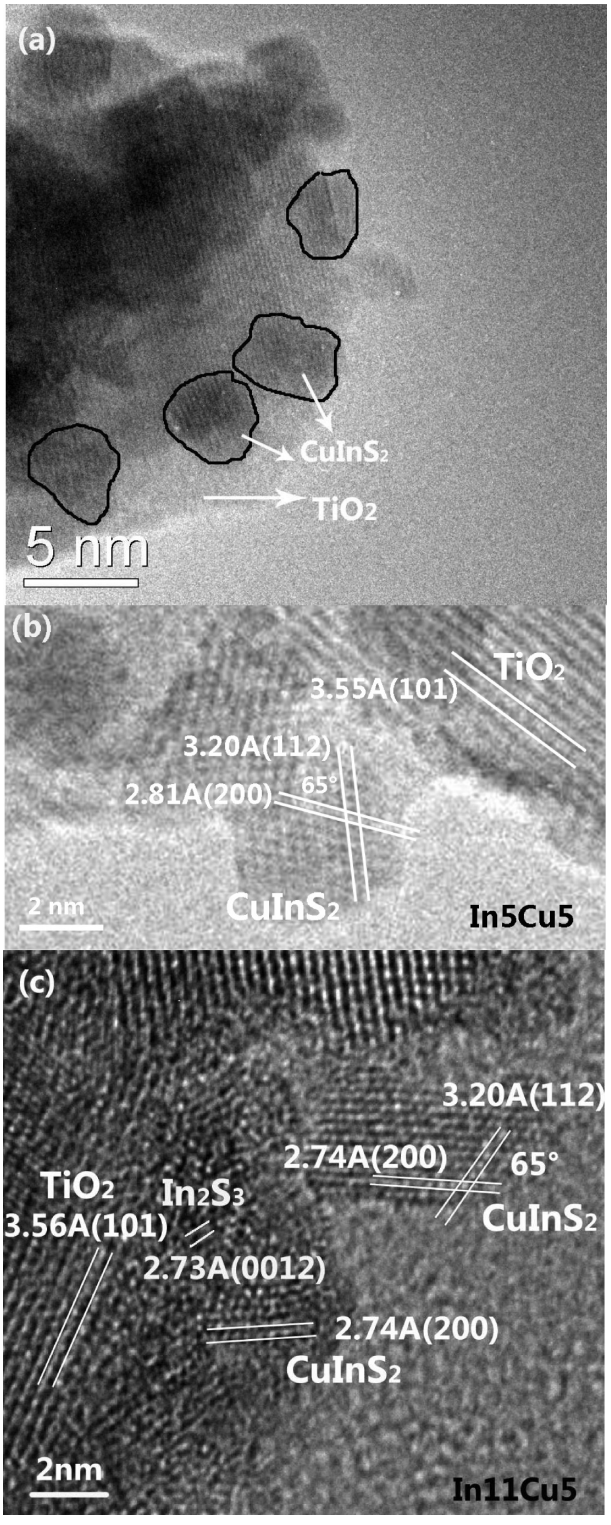

Figure 3. HRTEM images of the CIS-sensitized TiO_2 films: (a) In5Cu5, CIS nanoparticles are encompassed in black lines; (b) In5Cu5; (c) In11Cu5.

Figure 5 presents SEM images of the TiO_2 films before and after sensitization. It can be seen that the films for the In5Cu5 samples consisted of nanoparticles in sizes of ~20 nm, and the pores between the nanoparticles remained open compared with the films before sensitization. However, with an increase in the In−S deposition cycles, the nanoparticles tended to be aggregated and some of the pores were gradually blocked,

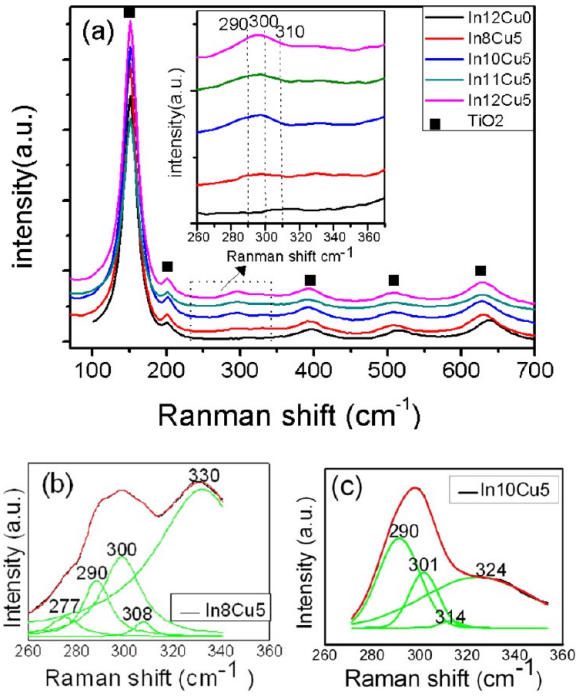

Figure 4. (a) Raman spectra of the sensitized TiO_2 with an exposure time of 2 s. Inset: spectra obtained with an exposure time of 6 s. Fitting curves of Raman peaks around 300 cm^{-1} for (b) In8Cu5 and (c) In10Cu5: original (black); fitted (blue); sum of the fitted curves (red).

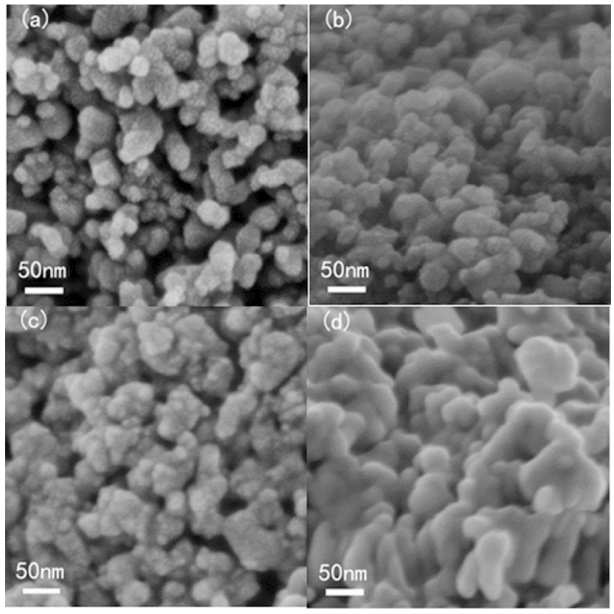

Figure 5. SEM images of mesoporous TiO_2 films: (a) before sensitization; (b) In5Cu5; (c) In10Cu5; (d) In12Cu5.

which indicated that the specific surface area of the sensitized TiO_2 films decreased with an increase in the In−S deposition cycles.

4.2. Photovoltaic Performance and Interface Recombination. In order to detect the light-harvesting property of the CIS-sensitized TiO_2 films, the diffuse absorption spectra of the samples have been obtained according to absorption (%) = 100% − transmittance − reflectance. Figure 6a shows the diffuse absorption spectra of the CIS-sensitized TiO_2 electrodes with different deposition cycles of In−S. The spectra for the

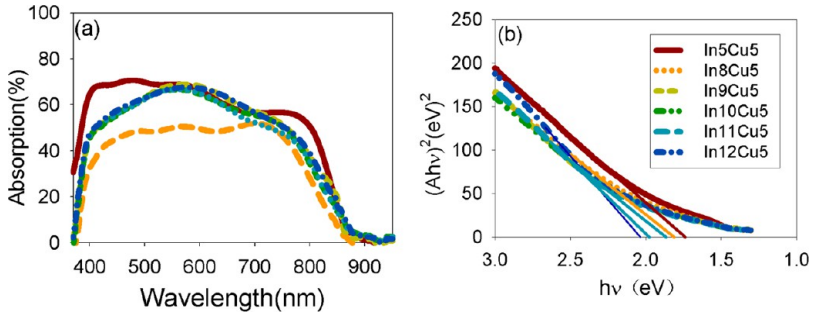

Figure 6. (a) Diffuse absorption spectra of the CIS-sensitized TiO_2 electrodes. (b) Plot of $(Ah\nu)^2$ as a function of the photon energy $(h\nu)$ for the sensitized TiO_2 films.

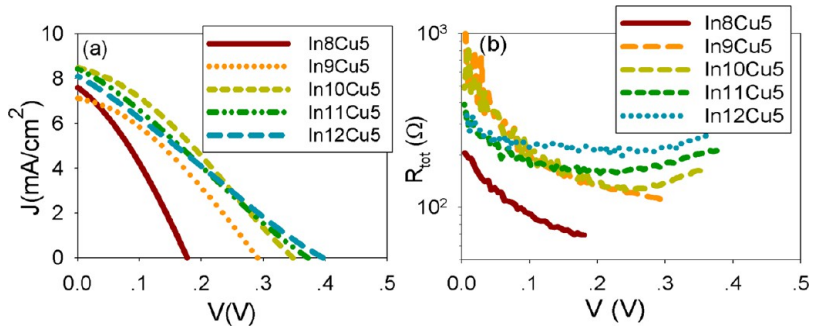

Figure 7. (a) $J-V$ curves of the CIS-sensitized solar cells with different numbers of In−S deposition cycles. (b) Total resistance, R_{tot}, of the cells derived from the $J-V$ curves.

Table 2. Photovoltaic Performance Parameters of CIS-Sensitized Solar Cells

	V_{oc} (V)	J_{sc} (mA cm^{-2})	FF	η (%)	$R_{se@V=E_\mu}$ (Ω)	R_{remin} (Ω)	$\ln(R_{re}/R_{remin})$ vs V relation	λ (eV)	E_μ (eV)	β
In5Cu5	0.03	0.63	0.27	0.005						
In8Cu5	0.18	7.61	0.31	0.43	33	36	$28.5(qV-0.20)^2$	0.34	0.20	0.30
In9Cu5	0.29	7.13	0.34	0.70	29	81	$29.7(qV-0.25)^2$	0.32	0.25	0.39
In10Cu5	0.35	8.49	0.31	0.92	27	98	$26.8(qV-0.24)^2$	0.36	0.24	0.34
In11Cu5	0.37	8.44	0.27	0.84	36	120	$14.2(qV-0.22)^2$	0.68	0.22	0.16
In12Cu5	0.40	8.15	0.25	0.82	32	166	$11.6(qV-0.20)^2$	0.83	0.20	0.13

In9Cu5, In10Cu5, In11Cu5, and In12Cu5 samples nearly overlapped with each other, indicating an average absorption capacity of around 55% ranging from 380 to 850 nm, which needed to be further improved; i.e., the thickness of the sensitized films needed to be optimized. The In5Cu5 samples owned a higher light absorption probably because they consisted of Cu-rich CIS. The In8Cu5 samples exhibited a lower light absorption capacity because they had a higher reflection, the reason for which was not very clear. In addition, Figure 6b presents variation of $(Ah\nu)^2$ as a function of the photon energy $(h\nu)$ for the sensitized TiO_2 films. A has been calculated according to following relationship:

$$A = -\log\frac{(1-R)^2}{T} \tag{10}$$

where T and R were the transmittance and reflectance of the CIS-sensitized TiO_2 films with the TiO_2 films as blanks. The values of the optical band edge, E_g, listed in Table 1 were estimated by extrapolating the linear portion to the x axis. For the In5Cu5 samples, the blue shift of the absorption edge relative to the bulk CIS (~1.5 eV) indicated that the grain size was in the quantum confinement region, and the grain size of ~5.6 nm was estimated according to the literature.[15] This value coincided with the result from HRTEM measurements but was much smaller than that obtained from XRD measurements. Compared with the In5Cu5 samples, the blue shift of the absorption edges with an increase in the In−S deposition cycles could be attributed to an increase in the thicknesses of In_2S_3 buffer layers because In_2S_3 has a band gap of about 2.1 eV.[22]

To investigate the photovoltaic performance of the solar cells, the photocurrent−voltage ($J-V$) curves for the CIS-sensitized solar cells with different deposition cycles of In−S have been measured, as shown in Figure 7a, and the performance parameters are listed in Table 2. The results showed that the open-circuit voltage, V_{oc}, of the cells increased with an increase in the In−S deposition cycles, which indicated that electron recombination has been apparently retarded with an increase in the In−S deposition cycles. However, the short-circuit photocurrent density, J_{sc}, and FF of the cells increased at first and then decreased. In order to obtain a deep understanding of this phenomenon, the electron recombination properties of the cells have been investigated.

For conventional DSCs, the dark current of the cells can be considered to be the recombination current. However, in the semiconductor-sensitized solar cells, the dark current of the cells (see Supporting Information S2) could be much lower than the recombination current under illumination because the holes in the semiconductor sensitizers play an important role in

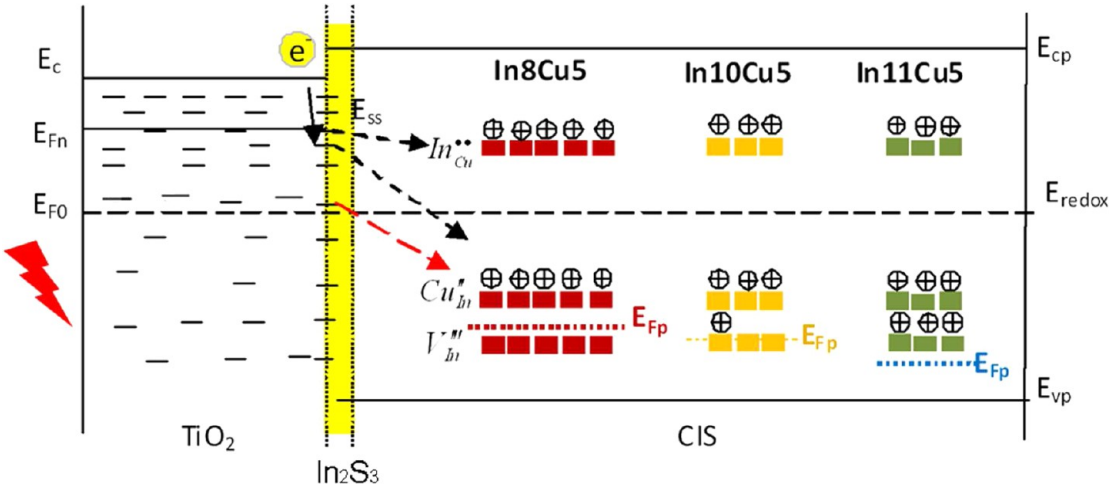

Figure 8. Schematic maps of the recombination between the electrons in TiO_2 captured by the surface states and the acceptors in CIS. Different densities of defect states for In8Cu5, In10Cu5, and In11Cu5 are depicted in red, yellow, and green ■, respectively. E_c and E_{cp} are the energy levels for the conduction bands of TiO_2 and CIS; E_{vp} is the valence band of CIS; E_{F0} is the quasi Fermi level of TiO_2 at 0 V or under dark conditions, which is equal to the Fermi level of the eletrolytes, E_{redox}; E_{Fp} is the quasi Fermi level of CIS, which is different from the others for the sample with different In−S deposition cycles.

the recombination, as reported by Mora-Sero et al.,[22] and the density of the holes in the semiconductor under dark conditions could be much lower than that under illumination conditions. For this reason, the recombination property of the cells should be investigated through the recombination resistance R_{re} under illumination. Accordingly, the total resistance, R_{tot}, of the cells was derived from the $J-V$ curves under light conditions according to following relationship:[23]

$$R_{tot} = \frac{dV}{d(J_{sc} - J)} \tag{11}$$

The total resistance R_{tot} of the cells consists of the total series resistance R_{se} and recombination resistance R_{re}, i.e., $R_{tot} = R_{se} + R_{re}$, and R_{se} can be expressed as a sum of the different contributions:

$$R_{se} = R_s + R_{ce} + \frac{1}{3}R_t + R_d \tag{12}$$

where R_s is the transport resistance of the TCO, R_t the electron-transport resistance in the TiO_2 electrode, R_d the diffusion resistance of the redox species, and R_{ce} the charge-transfer resistance of counter electrodes. R_{se} (R_d was not included) at different applied potentials under dark conditions has been obtained from electrochemical impedance spectroscopy measurements (see Supporting Information S3 and Figure S3.3), and the results show that R_{tot} could be considered to be R_{re}, i.e., $R_{re} \approx R_{tot}$ because R_{se} is much smaller than R_{re} and they had similar values for the samples with different In−S deposition cycles. Accordingly, Figure 7b presents the R_{tot} (or R_{re})$-V$ curves derived from $J-V$ curves in light. It can be seen that the recombination resistance at high potentials increased with the In−S deposition cycle, leading to an increase in V_{oc}. However, at low potentials, the recombination resistance increased at first and then decreased after the In−S deposition cycles achieved 10, which resulted in a decrease in FF of the solar cells for the In11Cu5 and In12Cu5 samples compared with the In10Cu5 samples. In order to confirm this judgment, the β value of the cells with different In−S deposition cycles has been estimated. It can be seen that R_{tot} (R_{re})$-V$ curves exhibited a parabolic shape, which well agreed with eq 4. From eq 4, we know that

$$\ln \frac{R_{re}}{R_{remin}} = \frac{(qV_F - E_\mu)^2}{4\lambda kT} \tag{13}$$

Through fitting of the $\ln(R_{re}/R_{remin})$ versus V curves (see Supporting Information S4), the values of E_μ and λ could be estimated. Furthermore, the value of β could be estimated according to eq 7. As shown in Table 2, the value of β increased at first and then decreased greatly after the number of In−S deposition cycles reached 10, which led to the same variation tendency of FF of the solar cells. However, one has to pay attention to the fact that the physical meaning of β for the semiconductor-sensitized solar cells might be identical with that for conventional DSCs because the electron recombination mechanism of the former is different from that of the latter, as indicated in the following text, which needs to be further investigated theoretically.

In order to reveal the nature of the above phenomenon, the electron recombination mechanism of the CIS-sensitized solar cells is investigated qualitatively here. The electron recombination mechanism in the inorganic semiconductor-sensitized solar cells is complicated, as indicated by Hodes[24] and our previous work.[25] Here we propose that the recombination in the CIS-sensitized solar cells is dominated by electron transfer from the conduction band of TiO_2 to the unoccupied defect states in CIS via the exponentially distributed surface states, as shown in Figure 8. As suggested by Hofhuis et al., the defect states in CIS consisted of In vacancies V_{In}''' (0.15 eV) and antisite defects Cu_{In}'' (0.25/0.20 eV) and $In_{Cu}^{\cdot\cdot\cdot}$ (1.15/1.10 eV).[26] To be expressed more vividly, in Figure 8, the defect states for In8Cu5, In10Cu5, and In11Cu5 are depicted in red, yellow, and green, respectively, with different densities of the states. It can be said that the recombination current density, J_{re}, is proportional to the density of the electrons in the surface states of TiO_2, n_e, and the density of unoccupied defect states in CIS, n_p. Besides, it is also proportional to the probability of electron transfer at TiO_2/CIS interfaces, ν_{el}. In another words, J_{re} has the following relationship with n_e, n_p, and ν_{el}:

$$J_{re}=qLn_e n_p \nu_{el} \quad (14)$$

With an increase in the In−S deposition cycle, the thickness of the In_2S_3 buffer layer increased, resulting in a decrease in the probability of electron transfer, ν_{el}, at TiO_2/CIS interfaces. It is clear that for the In5Cu5 samples the electron recombination current was much higher than that of the other samples because on the buffer layer existed a density of the defect states that was much higher, which led to the worst photovoltaic performance of the cells. When the In8Cu5 samples are compared with the In10Cu5 samples, the probability of electron transfer for the former is higher than that for the latter. In addition, the density of the defect states in the former is larger than that in the latter, which resulted in a higher J_{re} and hence a lower R_{re} for the In8Cu5 samples than the In10Cu5 samples at both high and low potentials, as shown in Figure 7b. On the other hand, with an increase in the In−S deposition cycle, the interface area between the sensitized TiO_2 and electrolyte decreased, leading to deceleration of the hole extraction from CIS to the electrolyte. As a result, the quasi Fermi level, E_{Fp}, of CIS shifted downward with an increase in the In−S deposition cycle, as shown in Figure 8. In a comparison of In11Cu5 with the In10Cu5 samples, at high potentials, because ν_{el} for In11Cu5 is lower than that for In10Cu5, electron recombination for the former is slower than that for the latter. However, at low potentials, the unoccupied defect states in CIS with energy levels below E_{F0} played an important role in the interface recombination. Although ν_{el} for In11Cu5 is lower than that for In10Cu5, the unoccupied defect states in CIS for In11Cu5 are higher than those for the In10Cu5 samples because of the downward shift of the quasi Fermi levels in CIS. As a result, electron recombination for In11Cu5 became faster than that for In10Cu5. This fact resulted in a decrease in R_{re} at low potentials and hence a decrease in the β value and FF for the In11Cu5 and In12Cu5 samples compared with the In10Cu5 samples.

In order to get more information on the electron recombination behavior of the solar cells, the electron lifetime of the cells, as shown in Figure 9, has been derived from open-circuit voltage decay (OCVD) measurement according to the following relationship:[27]

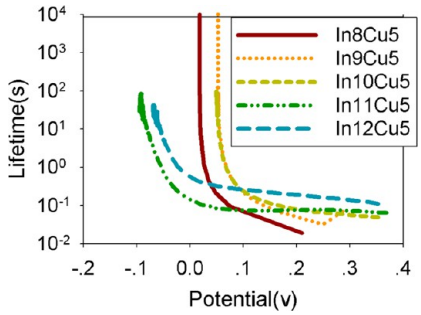

Figure 9. Electron lifetime of CIS-sensitized solar cells derived from OCVD measurement.

$$\tau = -\frac{kT}{e}\left(\frac{dV_{oc}}{dt}\right)^{-1} \quad (15)$$

where k is the Boltzmann constant and T is the absolute temperature. As shown in Figure 9, the electron lifetime, τ, had a variation tendency similar to that of R_{re} in light. At high potentials, the electron lifetime increased with an increase in the In−S deposition cycle. However, at lower potentials, the electron lifetime increased at first and then decreased after the number of In−S deposition cycles reached 10, which can be attributed to the same reasons as those described above.

Concerning J_{sc} of the solar cell, with an increase in the In−S deposition cycles, J_{sc} increased and achieved a maximum of ca. 8.49 mA cm^{-2} for In10Cu5 because of an increase in the crystallinity of CIS and a decrease in the electron recombination at the TiO_2/CIS interfaces. For In11Cu5 and In12Cu5, a decrease in J_{sc} can be attributed to an increase in the electron recombination at low potentials and a decrease in the grain size of CIS. In addition, it is found that the CIS-sensitized TiO_2 electrodes had higher photoeletrochemical stability (see Supporting Information S5) in the polysulfide electrolyte than the CdSe-sensitized TiO_2 electrodes did probably because of the higher stability of S^{2-} compared with Se^{2-}.

5. CONCLUSIONS

CIS nanoparticles have been successfully deposited onto the mesoporous TiO_2 films via the successive growth of In_xS and Cu_yS via the SILAR process and postdeposition annealing at 550 °C in vacuum with sulfur ambiance, which supply a new route for the fabrication of CIS-sensitized photoanodes. The CIS nanoparticles consist of tetragonal CIS composed of the chalcopyrite phase and Cu−Au ordering. When the deposition cycle of Cu−S was fixed, the grain size of tetragonal $CuInS_2$ increased with the deposition cycle of In−S at first, and then it tended to be constant. In the meantime, the composition of Cu−Au ordering decreased and a buffer layer of In_2S_3 formed at the TiO_2/CIS interface, which led to a decrease in the electron recombination at TiO_2/CIS interfaces. As a result, a relatively high efficiency of ca. 0.92% (V_{oc} = 0.35, J_{sc} = 8.49, and FF = 0.31) has been obtained. It is proposed that electron recombination in the CIS (or other semiconductor nanoparticle)-sensitized solar cells is dominated by electron transfer from the conduction band of TiO_2 to the unoccupied defect states in CIS via exponentially distributed surface states. Moreover, it has to be emphasized that the unoccupied defect states in CIS with energy levels below E_{F0} of the TiO_2 films play an important role in the interface electron recombination at low potentials and have great influence on FF of the solar cells. This is different from the conventional DSCs and needs to be further investigated theoretically. In future work, the density of the Cu−Au ordering and the defect states in CIS need to be further diminished to decrease the interface recombination. On the other hand, the pore structure and interface area of the sensitized TiO_2 films need to be further optimized to facilitate transfer of the holes from CIS to the acceptor in the electrolytes.

■ ASSOCIATED CONTENT

Ⓢ Supporting Information

XRD patterns, current−voltage curves, impedance spectra, series resistance of the CIS-sensitized solar cells, $\ln(R_{re}/R_{remin})$ versus V curves, stability of the CIS-sensitized solar cells with polysulfide as the electrolyte, and J−V curves. This material is available free of charge via the Internet at http://pubs.acs.org.

■ AUTHOR INFORMATION

Corresponding Authors

*E-mail: xuxq@ms.giec.ac.cn.
*E-mail: apjazs@cityu.edu.hk.

Notes

The authors declare no competing financial interest.

■ ACKNOWLEDGMENTS

This work was supported by the National Natural Science Foundation of China (Projects 21073193 and 21273241), by GRF Project 102810 from the Research Grants Council of Hong Kong, and by the Centre for Functional Photonics of the City University of Hong Kong.

■ REFERENCES

(1) Dittrich, T.; Belaidi, A.; Ennaoui, A. *Sol. Energy Mater. Sol. Cells* **2011**.
(2) Kamat, P. V. *J. Phys. Chem. C* **2008**, *112* (48), 18737−18753.
(3) Yu, W. W.; Qu, L.; Guo, W.; Peng, X. *Chem. Mater.* **2003**, *15* (14), 2854−2860.
(4) Tell, B.; Shay, J.; Kasper, H. *Phys. Rev. B* **1971**, *4* (8), 2463.
(5) Chang, C. H.; Lee, Y. L. *Appl. Phys. Lett.* **2007**, *91* (5), 053503−053503-3.
(6) Valkonen, M. P.; Kanniainen, T.; Lindroos, S.; Leskelä, M.; Rauhala, E. *Appl. Surf. Sci.* **1997**, *115* (4), 386−392.
(7) Zhang, Q.; Xu, T.; Butterfield, D.; Misner, M. J.; Du Yoel, R.; Emrick, T.; Russell, T. P. *Nano Lett.* **2005**, *5* (2), 357−361.
(8) Lutz, T.; MacLachlan, A.; Sudlow, A.; Nelson, J.; Hill, M. S.; Molloy, K. C.; Haque, S. A. *Phys. Chem. Chem. Phys.* **2012**, *14* (47), 16192−16196.
(9) Bisquert, J.; Zaban, A.; Salvador, P. *J. Phys. Chem. B* **2002**, *106* (34), 8774−8782.
(10) Luo, J.; Wei, H.; Huang, Q.; Hu, X.; Zhao, H.; Yu, R.; Li, D.; Luo, Y.; Meng, Q. *Chem. Commun.* **2013**, *49* (37), 3881−3883.
(11) Feng, J.; Han, J.; Zhao, X. *Prog. Org. Coat.* **2009**, *64* (2-3), 268−273.
(12) Nanu, M.; Schoonman, J.; Goossens, A. *Adv. Funct. Mater.* **2005**, *15* (1), 95−100.
(13) Wu, J. J.; Jiang, W. T.; Liao, W. P. *Chem. Commun.* **2010**, *46* (32), 5885−5887.
(14) Chang, H. Y.; Tzeng, W. J.; Lin, C. H.; Cheng, S. Y. *J. Alloys Compd.* **2011**.
(15) Zhong, H. Z.; Zhou, Y.; Ye, M. F.; He, Y. J.; Ye, J. P.; He, C.; Yang, C. H.; Li, Y. F. *Chem. Mater.* **2008**, *20* (20), 6434−6443.
(16) Fabregat-Santiago, F.; Bisquert, J.; Garcia-Belmonte, G.; Boschloo, G.; Hagfeldt, A. *Sol. Energy Mater. Sol. Cells* **2005**, *87* (1-4), 117−131.
(17) Wang, Q.; Ito, S.; Gratzel, M.; Fabregat-Santiago, F.; Mora-Sero, I.; Bisquert, J.; Bessho, T.; Imai, H. *J. Phys. Chem. B* **2006**, *110* (50), 25210−25221.
(18) Ranjith, R.; John, T. T.; Sudha Kartha, C.; Vijayakumar, K. P.; Abe, T.; Kashiwaba, Y. *Mater. Sci. Semicond. Process.* **2007**, *10* (1), 49−55.
(19) Djordjevic, J.; Pietzker, C.; Scheer, R. *J. Phys. Chem. Solids* **2003**, *64* (9-10), 1843−1848.
(20) Oja, I.; Nanu, M.; Katerski, A.; Krunks, M.; Mere, A.; Raudoja, J.; Goossens, A. *Thin Solid Films* **2005**, *480*, 82−86.
(21) Spasevska, H.; Kitts, C. C.; Ancora, C.; Ruani, G. *Int. J. Photoenergy* **2012**.
(22) Gonzalez-Pedro, V.; Xu, X.; Mora-Sero, I.; Bisquert, J. *ACS Nano* **2010**, *4* (10), 5783−5790.
(23) Fabregat-Santiago, F.; Bisquert, J.; Palomares, E.; Otero, L.; Kuang, D.; Zakeeruddin, S. M.; Grätzel, M. *J. Phys. Chem. C* **2007**, *111* (17), 6550−6560.
(24) Hodes, G. *J. Phys. Chem. C* **2008**, *112* (46), 17778−17787.
(25) Hetsch, F.; Xu, X.; Wang, H.; Kershaw, S. V.; Rogach, A. L. *J. Phys. Chem. Lett.* **2011**, *2*, 1879−1887.
(26) Hofhuis, J.; Schoonman, J.; Goossens, A. *J. Phys. Chem. C* **2008**, *112* (38), 15052−15059.
(27) Bisquert, J.; Zaban, A.; Greenshtein, M.; Mora-Seró, I. *J. Am. Chem. Soc.* **2004**, *126* (41), 13550−13559.